On the role of sidewalls in the transition from straight to sinuous bedforms

N. Zgheib[1,2], and S. Balachandar[2]

[1]School of Engineering, Lebanese American University, Byblos, Lebanon.

[2]Department of Mechanical and Aerospace Engineering, University of Florida, Gainesville, FL 32611, USA.

Corresponding author: Nadim Zgheib (nadim.zgheib@lau.edu.lb)

Key Points:

- Lateral sidewalls significantly increase crestline sinuosity.
- Influence of lateral domain extent on sinuosity is small but noticeable.
- Influence of lateral extent is amplified in the presence of sidewalls.

Abstract

We present results from direct numerical simulation (DNS) on the transition from straight-crested to sinuous-crested bedforms. The numerical setup is representative of turbulent open channel flow over an erodible sediment bed at a shear Reynolds number of $Re_\tau = 180$. The immersed boundary method (IBM) accounts for the presence of the bed. The simulations are two-way coupled such that the turbulent flow can erode and modify the bed, and in turn, the bed modifies the overlying flow. Coupling from the flow to the bed occurs through the Exner equation, while back coupling from the bed to the flow is achieved by imposing the no-slip and no-penetration condition at the immersed boundary. The simulation setup is similar to that by *Zgheib et al.* [2018a] except for the presence of sidewalls to better mimic laboratory flume conditions. Sidewalls are observed to significantly increase bedform sinuosity.

1 Introduction

Bedforms are fascinating features of multiphase flows where overlying flow continuously works and modifies an underlying erodible sediment bed [e.g. *Blondeaux,* 1990; *Ouriemi et al.,* 2009]. Depending on flow conditions and sediment properties, multiple scenarios for bed formation are possible [e.g. *Kennedy,* 1969]. When the resulting bed stress slightly exceeds the critical shear stress necessary for sediment incipient motion, and when sediment size is of the order of a few hundred microns or smaller, ripples generally form [*Charru et al.,* 2013*]*. Ripples possess an asymmetric triangular profile along the flow direction. The slope downstream of the crest, along the lee side, is relatively steep and usually corresponds to the sediment angle of repose [*Coleman and Melville,* 1996]. Alternatively, the slope on the stoss side is relatively mild. Once fully developed, ripples usually attain a self-similar profile where slopes on the stoss and lee sides remain nearly unchanged as the ripple height varies [e.g. *Yalin,* 2013; *Zgheib et al*., 2018b].

In laboratory experiments s, the stages of ripple evolution from a flat bed are well documented [e.g. *Baas,* 1994; *Venditti et al*., 2005]. The process is divided into 5 stages: (i) Longitudinal streaks corresponding to the imprints of the overlying turbulent flow initially appear. (ii) Then, due to the instability of the bed, quasi-spanwise structures composed of a few grains emerge and evolve into chevron features, which coalesce to form (iii) incipient crestlines. Incipient crestlines grow and coarsen resulting in (iv) straight/sinuous ripples termed developing ripples. These developing ripples continue to grow and develop until they reach a stationary/equilibrium state and become (v) fully developed ripples.

Recently, numerical simulations have become a popular tool for studying bed formation. These include particle-resolved DNS [e.g. *Kidanemariam and Uhlmann,* 2014; 2017], as well as simulations that resolve the flow but model the bed through a point-particle approach [e.g. Sun and Xiao, 2016] or through the Exner equation [e.g. *Chou and Fringer,* 2010; *Sotiropoulos and Khosronejad,* 2016]. Currently, fully resolved DNS or DNS with some degree of modelling for the bed, have been unable to produce sinuous-crested bedforms. Fully developed bedforms from such simulations [e.g. *Kidanemariam and Uhlmann,* 2014; 2017, *Zgheib et al*. 2018, a;b] have remained largely two-dimensional, i.e. bedform crestlines remain straight.

There could be many reasons why bedforms from DNS remain straight-crested while their counterparts in experiments transition to sinuous-crested bedforms. One such reason could be the width of the numerical domain. The secondary instability (i.e. transition from straight to sinuous bedforms) could be hindered by the size of the numerical domain if the latter is sufficiently restrictive. Another aspect potentially responsible for the transition to sinuous bedforms is the

spatio-temporal variation in the ambient flow rate. Finally, the majority of simulations enforce periodicity on lateral boundaries of the numerical domain.. However, *Langlois and Valance* [2007] have suggested that sidewalls could be responsible for the aforementioned sinuosity. Sidewalls result in corner-induced secondary circulations and near-wall reductions in bed stress/transport capacity, which could potentially create sinuous crestlines.

Since sinuous ripples are the norm in laboratory experiments and field observations it is of importance to capture them in numerical simulations in order to understand the fundamental mechanisms of their formation. When simulations fail to reproduce such features, it is important to pinpoint missing physics in these simulations that could remedy such a failure. It is thus the objective of this study to investigate the sinuosity of crestlines by testing the effects of the numerical extent of the domain as well as the presence and properties of sidewalls.

The purpose of this work is to show that coupled bed flow direct numerical simulations can in fact produce sinuous-crested bedforms and that sidewalls may be primarily responsible for the transition from straight-crested to sinuous-crested bedforms. We choose the simulation setup to be identical to the recent setup employed by *Zgheib et al*. [2018 a;b] where developed bedforms remain straight-crested. The two setups however differ in that the present simulations use immersed boundary methodology to employ laterally confining sidewalls to test their effect on the transition from straight to sinuous bedforms. Additionally, the lateral extent for some simulations is expanded by a factor of three to test the effect of domain size. With the laterally expanded domain, the bedform width-to-height ratio is around 100.

2 Mathematical Model

The numerical setup is shown in

Figure 1. The channel is periodic along the flow direction and is confined by sidewalls. The setup corresponds to turbulent open channel flow over a time-evolving complex topography, i.e. the sediment bed. The presence of the bed is accounted for through the immersed boundary method of *Uhlmann* [2005] where the no-slip and no-penetration velocity boundary condition is imposed at the immersed boundary, i.e. the sediment bed. In applying these velocity boundary conditions, the permeability of the bed has been neglected. In reality, the bed is porous, which influences the near wall dynamics due to the penetration of turbulence into the pores [e.g. Marion et al., 2002; Packman et al., 2004; Cardenas and Wilson, 2007]. Such microscale physics are not accounted for in our simulations and may influence bedform evolution.

We solve the following conservation equations using a pseudo spectral code [*Cortese and Balachandar,* 1995; *Shringarpure et al.,* 2012].The temporal and spatial evolution of the bed is governed by the Exner equation (3) [*Cayocca, 2001*; *Ancey, 2010*].

$$\nabla \cdot \boldsymbol{u} = 0\,, \tag{1}$$

$$\frac{D\boldsymbol{u}}{Dt} = \boldsymbol{e}_x - \nabla p + \frac{1}{Re_\tau}\nabla^2 \boldsymbol{u} + \boldsymbol{f}, \tag{2}$$

$$\varphi \frac{\partial \eta}{\partial t} = -\nabla \cdot \boldsymbol{q} + \varepsilon \langle |\boldsymbol{q}| \rangle \nabla^2 \eta\,. \tag{3}$$

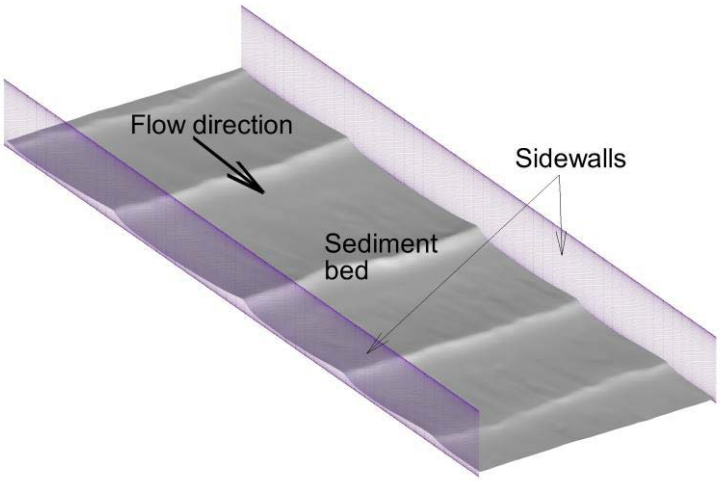

Figure 1. Numerical domain showing laterally confining sidewalls and the time-evolving bed.

In equations (1) and (2), $\boldsymbol{u}$ represents the three-dimensional flow field, $\boldsymbol{e}_x$ is a unit vector in the streamwise x-direction corresponding to the non-dimensional mean pressure gradient. p is the perturbation pressure and $\boldsymbol{f}$ is the IBM coupling force between the flow and the bed that enforces the no-slip and no-penetration condition at the bed. Re_τ is the shear Reynolds number based on average bed shear velocity U_τ^*, mean flow depth H_f^*, and kinematic viscosity of water ν^*. Here, the asterisk denotes a dimensional quantity, all other variables are non-dimensional. The length and velocity scales adopted are H_f^* and U_τ^*, respectively. The time scale corresponds to their ratio H_f^*/U_τ^*.

In equation (3), η denotes the bed height, φ the sediment volume fraction, $\boldsymbol{q}$ the sediment flux vector, and ε is an adjustable parameter [*Cayocca, 2001*] that controls numerical diffusion. The sediment flux is computed from the bed stress using the *Wong and Parker* [2006] modified *MPM* [1948] relationship. The values of $\varphi = 0.6$ and $\varepsilon = 4$ are identical to those used in *Zgheib et al*. [2018 a;b]. Additional details on the time integration of the governing equations and the numerical implementation of the immersed boundary method are available in *Akiki and Balachandar* [2016] and *Zgheib et al*. [2018a].
We consider one of the straight-crested simulations of *Zgheib et al*. [2018a] as a benchmark case and conduct five new simulations. In each new simulation, we vary one aspect such as domain width, lateral boundary conditions, sediment flux profile, or grid resolution. By varying only one aspect in each simulation, we can identify and isolate its influence. Details of the simulations are shown in Table 1. The terms ND and WD correspond to narrow domain and wide domain, respectively. These differ only by the lateral extent, where the wider domain is three times wider.

The dimensions of the narrow domain are identical to the simulations of *Zgheib et al*. [2018a]. The letters S and P denote the type of lateral boundary condition, where S indicates the presence of sidewalls and P indicates the use of periodic conditions. The subscript HR indicates the simulation has twice as fine a resolution in the lateral direction, while the subscript Flux denotes an artificial reduction in the near-bank sediment flux.

We note that the Reynolds number considered is modest and therefore smaller than those encountered in many real-world applications. The flow is strongly turbulent when the bedforms are small and the sediment bed is nearly flat. However, at later stages when developing ripples emerge, we find the logarithmic-law profile to be valid within a reduced region of the domain indicating that turbulence has somewhat weakened. Nevertheless, as bedforms evolve and the macroscopic roughness of the bed increases, we find the velocity profile to follow a trend similar to open-channel flows with small-scale roughness [Nikuradse, 1933].

Table 1. List of simulations. $d_p^* = 150\mu m$, $\rho_p^* = 1.57 g/cm^3$, and $\rho_f^* = 1.00 g/cm^3$ correspond to the particle diameter, particle density, and fluid density, respectively. The average bed stress and mean flow depth are designated by $U_\tau^* = 1.237 cm/s$ and $H_f^* = 1.455 cm$, respectively. All five values are the same across all simulations. $L_x \times L_y \times L_z$ and $N_x \times N_y \times N_z$ denote the size and grid resolution of the domain along the streamwise, spanwise, and vertical directions, respectively. All simulations are run at $Re_\tau = 180$.

Simulation name	$L_x \times L_y \times L_z$	$N_x \times N_y \times N_z$
ND-P	$12 \times 4 \times 1.05$	$288 \times 96 \times 301$
ND-S	$12 \times 4 \times 1.05$	$288 \times 96 \times 301$
$\mathrm{ND_{HR}S}$	$12 \times 4 \times 1.05$	$288 \times 192 \times 301$
$\mathrm{ND_{Flux}}$-P	$12 \times 4 \times 1.05$	$288 \times 96 \times 301$
WD-S	$12 \times 12 \times 1.05$	$288 \times 288 \times 301$
WD-P	$12 \times 12 \times 1.05$	$288 \times 288 \times 301$

3 Results and Discussion

Recall that we ran five new simulations in addition to the benchmark simulation ND-P of *Zgheib et al*. [2018a]. In each new simulation, only one aspect is varied with respect to the benchmark simulation. In this section, we will first qualitatively test the influence of sidewalls and width of the domain on the sinuosity of crestlines. We will do so through side-by-side comparisons of the bed. The comparison is between the benchmark simulation on one hand and the ND-S (narrow domain with sidewalls to test the influence of sidewalls), WD-P (wide domain with laterally periodic boundary conditions to test the influence of domain width), and WD-S (wide domain with sidewalls to test the combined influence of sidewalls and domain width) simulations on the other hand. We will then investigate the influence of artificially reducing the near-bank sediment flux to identify the aspects of the boundary condition that create sinuosity. Finally, we provide a quantitative measure of sinuosity by measuring the root mean square variation of crestlines along the spanwise direction.

3.1 Influence of Sidewalls

To quantify the influence of sidewalls, we compare crestline profiles from present simulations to those from the benchmark simulation of *Zgheib et al*. [2018a]. Since we are only interested in the transition of the crestline profile in developing ripples from a straight to a sinuous profile, we will test the effect of sidewalls at a point in the simulations when the ripples have

entered a developing state. That is, the present simulations will not start with a flat bed, but rather, the starting point of all simulations will correspond to the laterally periodic simulation of *Zgheib et al*. [2018a] at $t = 750$ where the ripples profiles have become self-similar. It is at this time that variations such as the presence of sidewalls, the width of the domain, the finer grid resolution, and the modified sediment flux profile are implemented.

Simulations are then run for a sufficient time such that initial conditions are forgotten. We should note here that the aforementioned time corresponds to non-dimensional bulk time defined as $t = t^* U_b^*/H_f^*$, where the dimensional bulk velocity at the start of the simulation U_b^* is defined as

$$U_b^* = \frac{1}{H_f^* \; L_y^*} \int_0^{H_f^*} \int_0^{L_y^*} u^* \, dy^* \, dz^* \approx 15.6 U_\tau^* \, . \tag{4}$$

In fact, throughout the manuscript, time will be given in bulk time units unless otherwise stated.

To investigate the effect of sidewalls in ND-S, we first consider the laterally periodic ND-P simulation from *Zgheib et al*. [2018a] and introduce sidewalls at $t = 750$, a time when the sediment bed has become spanwise invariant with straight-crested developing ripples. The sidewalls could have been introduced at the start of the simulation, however they are introduced at $t = 750$ for two main reasons. First, prior to this time, the bed is largely three-dimensional due to the presence of numerous defects, and second it is after this time that ripples enter the developing state and become straight crested with no signs of ever transitioning to sinuous-crested ripples. Since we are interested in the transition of these developing ripples into sinuous ripples, we only introduce the sidewalls at $t = 750$. Starting at $t = 750$ has also the added benefit of saving computational time. After imposing the new lateral boundary condition, we continue to run the simulation and monitor the changes the sidewalls impose on the ripples. We show in Figure 2 panels a) through d) a top view of the bed from ND-S and ND-P at two time instances, namely $t = 1300$ and $t = 1840$. We observe that the sidewalls have made the ripple crestlines more sinuous. However, at any time instance, the degree of sinuosity varies from one ripple to another. For example at $t = 1300$, we find the 2$^{\text{nd}}$ ripple from the left to be the most sinuous compared to the other three ripples. We also observe that the sinuous crestlines may exhibit infection points as in the two leftmost ripples at $t = 1840$.

Finally, we note that the same mean streamwise pressure gradient drives the flow in all simulations. Consequently, for simulations with sidewalls, the sidewall drag due to the no-slip condition reduces the net pressure gradient available to drive the flow. This in turn reduces the bed stress and consequently results in more slowly advancing ripples. This explains why sinuous ripples advance slower than their straight-crested counterparts.

3.2 Influence of a Wider Numerical Domain

The purpose behind the WD-P simulation is to test whether the transition to sinuous-crested bedforms, in laterally periodic simulations, was hindered by the numerical domain width. To that end, the lateral extent of the WD-P simulation was expanded by a factor of three, so that with the wider domain, the width-to-height ratio of the ripples becomes approximately 100.

Here again we start the simulation from ND-P at $t = 750$ and exploit the periodic nature of the simulation to duplicate the domain three times in the lateral direction. We find the larger

width of the domain to have a small but noticeable influence on crestline sinuosity, however not to the same extent as seen with the presence of sidewalls.

3.3 Combined Influence of Sidewalls and a Wider Numerical Domain

We thus observe from sections 3.1 and 3.2 that sidewalls and domain width do influence crestline sinuosity. The effect of the former is however more important than the subtle influence of the latter. However, when both aspects are combined in one simulation, as in the case of the ND-S simulation, we observe crestline sinuosity to be amplified. In Figure 2 panels e) and f), we show a top view of the bed from ND-S and WD-S at $t = 2500$. The combined influence of sidewalls and a wider domain are readily visible especially near the sidewalls. The colored image in panel g) is taken from *Paull et al.* [2010] and corresponds to field observations of sinuous-crested bedforms within the axial channel of the Monterey Canyon. While the field observations are for much larger bedforms, we do observe similarities in the shape of crestlines. For example, we observe the crestline of the bedforms pointed to by the red arrow to be nearly flat around the center of the channel and extend the farthest downstream near the edge of the channel. Alternatively, we find the crestline of the bedforms pointed to by the purple arrow to have a smooth spanwise variation. Furthermore, due to the lateral confinement in the channel, we find the slope of bedforms to progressively attain smaller values (such that the crestlines become difficult to identify) near the lateral edges. This is similar to what we observe in the present simulations due to sidewalls.

While the beds in panels e) and f) correspond to the same time instance and both comprise four ripples, the streamwise location of these ripples are markedly different from one bed to the other. For example, the crestline from the first ripple from the bottom in ND-S is located near $x = 3.2$, while that from WD-S is located near $x = 1.2$. This is in contrast with the similarity of the laterally periodic simulations ND-P and WD-P (not shown here). The difference must be due to sidewalls (since it is the only aspect that has been modified). Recall that the simulations are solely driven by a mean streamwise pressure gradient, ΔP. Recall also that sidewalls, because of the no-slip condition, reduce the portion of the pressure gradient available to drive the flow. If we label the loss of pressure gradient with the presence sidewalls as ΔP_S, then

$$\left.\frac{\Delta P_S}{\Delta P}\right|_{\mathrm{WD-S}} < \left.\frac{\Delta P_S}{\Delta P}\right|_{\mathrm{ND-S}} . \tag{5}$$

That is, losses due to sidewalls are smaller in the wider domain than in the narrower domain, which results in the aforementioned difference in Figure 2.

3.4 Quantitative Measure of Crestline Sinuosity

To obtain a quantitative measure of sinuosity, we measure the standard deviation of x_c (the spanwise-dependent streamwise location of the crestline) about its mean value $\bar{x}_c$. The standard deviation for each crestline is defined as

$$s_x = \frac{1}{N_y}\sum_{j=1}^{N_y}\sqrt{(x_c(j) - \bar{x}_c)^2} . \tag{6}$$

Here N_y represents the number of grid points in the spanwise direction. Equation (6) pertains to one of the multiple ripples present in the domain at any time instance. To obtain a single value of s_x for the entire bed (and not just for a specific ripple), we average s_x over all ripples at each time instance to obtain $\bar{s}_x(t)$.

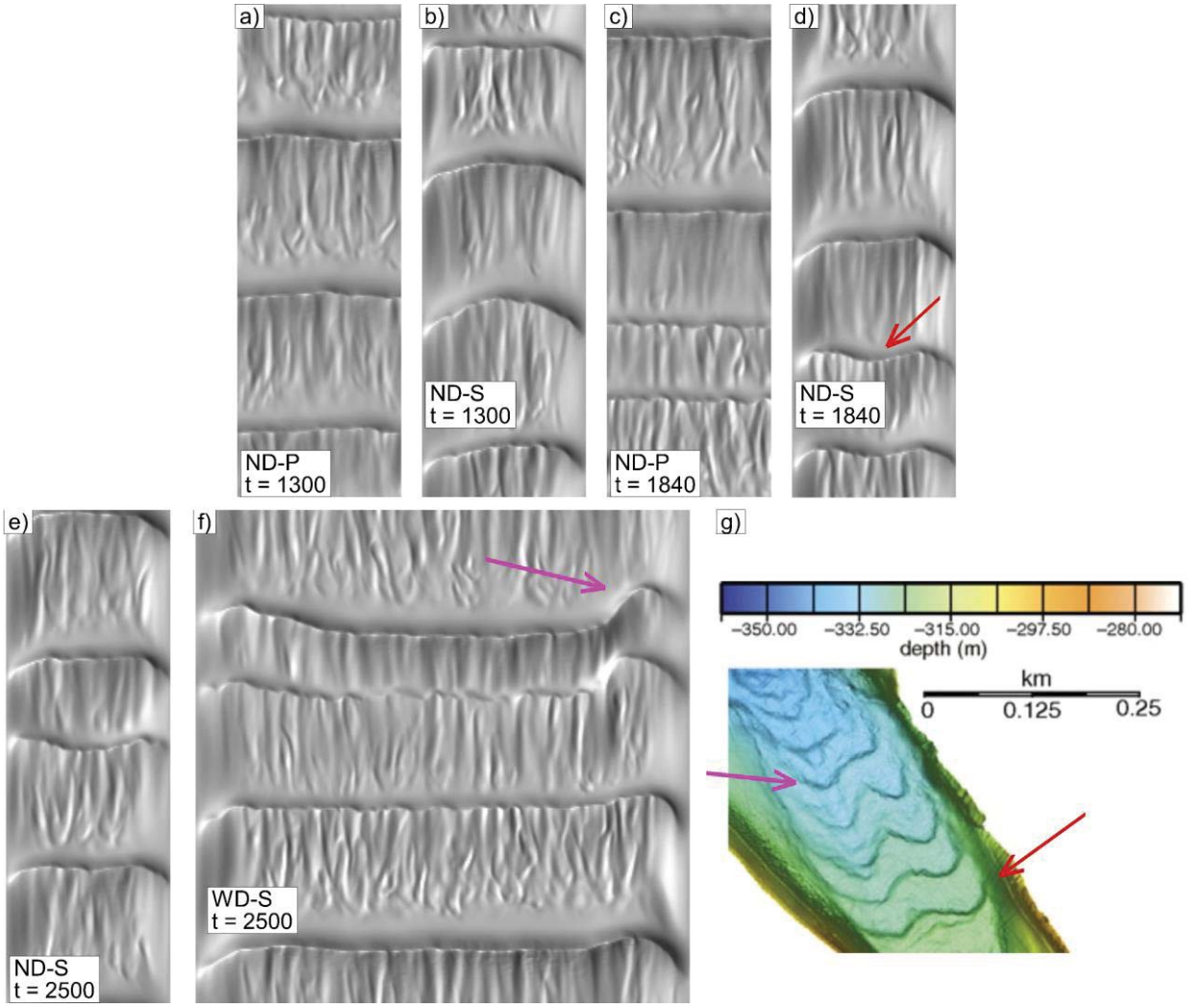

Figure 2. a) - d) Top view of the bed from ND-S and ND-P at $t = 1300$ and $t = 1840$. The crestlines for the four bedforms in ND-S show various degrees of sinuosity, whereas those from ND-P remain predominantly straight. Flow is from bottom to top. e) - f) Top view of the sediment bed from ND-S and WD-S at $t = 2500$. The wider domain induces a significant increase in crestline sinuosity. Flow is from bottom to top. The image in panel g) is taken from field observations of *Paull et al.* [2010]. The red and purple arrows point to crestline similarities for the bedforms in question. Flow is from top to bottom.

In Figure 3, we plot the temporal evolution of $\bar{s}_x$. As mentioned earlier, simulations start from $t = 750$. For the laterally periodic, benchmark simulation ND-P, we observe $\bar{s}_x$ to remain relatively small and to never exceed a value of 0.05 for $t > 1500$. The small but noticeable

difference due to the wider domain is manifested in a small but noticeable rise in $\bar{s}_x$ for WD-P. The increase in $\bar{s}_x$ is largest toward the end of the simulation at $t = 2500$.

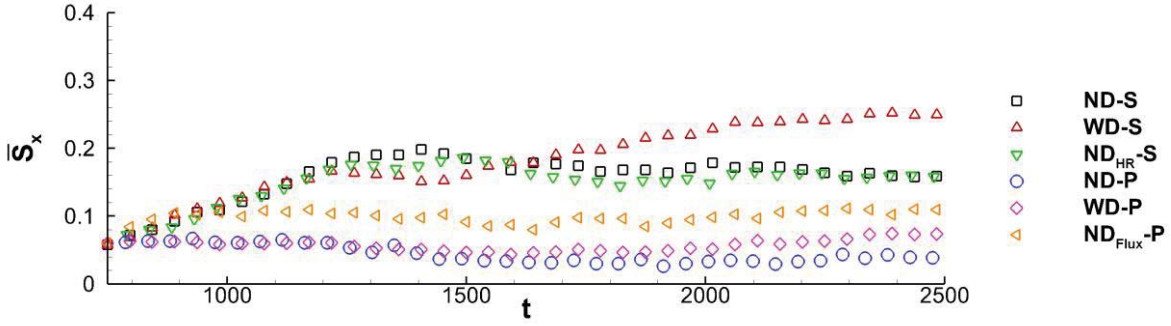

Figure 3. Mean rms fluctuation versus time. Sidewalls visibly increase crestline sinuosity (ND-S). Domain width enhances sinuosity (WD-P), especially in the presence of sidewalls (WD-S). Artificially reducing the near-bank sediment flux does increase sinuosity even in the absence of sidewalls (ND_{Flux}-P).

Similarly, we can clearly identify the increase in sinuosity in ND-S compared to ND-P. On average, for $t > 1500$, we find $\bar{s}_x$ to be five times larger than the corresponding mean value for ND-P. Additionally, when sidewalls are added to the wider domain simulation (WD-S), we find $\bar{s}_x$ to attain even larger values than those for the ND-S. This is in agreement with the qualitative results from section 3.3. In fact, beyond $t = 1750$, we observe the combined effects of a wider domain and the presence of sidewalls to exceed the sum of individual effects. That is

$$\bar{s}_x|_{\mathrm{WD-S}} > \bar{s}_x|_{\mathrm{ND-S}} + \bar{s}_x|_{\mathrm{WD-P}} . \tag{7}$$

To make sure the simulations remain grid independent in the presence of sidewalls, we ran the ND_{HR}-S simulation. This simulation has twice the grid resolution along the spanwise y-direction as compared to the other simulations. We observe no variation in the shape of the bed. This is further confirmed from the temporal variation of $\bar{s}_x$ in Figure 3.

3.5 Effects of Artificially Reducing the Near-Bank Sediment Flux

It is clear from the simulations that sidewalls significantly influence the transition from straight-crested to sinuous-crested bedforms. It is not clear however whether this transition is due for instance to corner-induced secondary circulation or to reduction in near-bank sediment flux, or to both. Corner-induced secondary circulation may create three-dimensional sediment patterns and modify bed topology through the formation of ridges [e.g. *Nezu and Nakagawa,* 1984; *McLelland et al.,* 1999]. Moreover, a reduction in near-bank sediment flux is often used to mimic the presence of sidewalls in simple morphodynamic models [e.g. *Stam,* 1997; *Jerolmack and Mohrig,* 2005].

The purpose of the ND_{Flux}-P simulation is to characterize the influence of secondary circulation and near-bank flux reduction. We isolate the latter effects by considering a laterally periodic simulation and artificially reducing the bed stress (and consequently the sediment flux) near the lateral edges of the domain. We define a scaling function $\chi(y)$ that is 0 at the lateral

boundaries, but smoothly increases to 1 within a narrow region away from the lateral boundaries. This scaling function has the form

$$\chi(y) = \tanh(cy)\tanh\left[c\left(L_y - y\right)\right]. \tag{8}$$

In equation (8), c is a constant that controls the thickness of the region where $\chi(y)$ transitions from 0 to 1, and consequently where the bed stress is reduced. The larger the value for c, the narrower the transition region becomes. We set $c = 7$ so that χ mimics the profile of the time and streamwise averaged x-component of bed stress τ_x from ND-S. Note that lateral boundaries are at $y = \{0, L_y\}$.

As shown in Figure 3, a reduction in near-bank sediment flux does increase crestline sinuosity, albeit not to the full extent as with the presence of sidewalls. This implies that corner-induced secondary circulation and near-bank sediment flux reduction are both likely responsible for creating sinuous-crested bedforms.

4 Conclusions

We investigated the effects of sidewalls and domain width on ripple crestline sinuosity in the context of direct numerical simulations. We ran five simulations and in each varied one aspect with respect to the benchmark simulation of *Zgheib et al*. [2018 a;b] to isolate and examine its influence on sinuosity. key aspects that we investigated include lateral boundary conditions, domain width, lateral grid resolution, and a modified bed stress profile. In the benchmark simulation, crestlines remained fairly straight.

We observe the presence of sidewalls to significantly increase crestline sinuosity, whereas an increase in domain width, with laterally periodic boundary conditions, to result in a small but noticeable increase in small-scale undulations. However, when sidewalls are added to a wider domain, we find the sinuosity to be amplified. That is, the increase in sinuosity with the two aspects combined was greater than the increase in sinuosity for each aspect applied separately. We also find that near-bank sediment flux reduction and corner-induced secondary circulation are both likely responsible for the creation of sinuous-crested bedforms.

Acknowledgments

We are grateful to ExxonMobil Upstream Research Company for providing support through grant number EM09296. We are also grateful to the anonymous reviewers for their insightful comments and thorough inspection that improved the quality of the paper. Numerical data presented herein will be available in the Sediment Experimentalists Network (SEN) Knowledge Base (http://www.sedexp.net).

References

Akiki, G., and Balachandar, S. (2016). Immersed boundary method with non-uniform distribution of Lagrangian markers for a non-uniform Eulerian mesh. Journal of Computational Physics, 307, 34-59. https://doi.org/10.1016/j.jcp.2015.11.019

Ancey, C. (2010). Stochastic modeling in sediment dynamics: Exner equation for planar bed incipient bed load transport conditions. Journal of Geophysical Research: Earth Surface, 115(F2). https://doi.org/10.1029/2009JF001260

Baas, J. H. (1994). A flume study on the development and equilibrium morphology of current ripples in very fine sand. Sedimentology, 41(2), 185-209. https://doi.org/10.1111/j.1365-3091.1994.tb01400.x

Blondeaux, P. (1990). Sand ripples under sea waves Part 1. Ripple formation. Journal of Fluid Mechanics, 218, 1-17. https://doi.org/10.1017/S0022112090000908

Cardenas, M. B., and Wilson, J. L. (2007). Dunes, turbulent eddies, and interfacial exchange with permeable sediments. *Water Resources Research*, *43*(8). https://doi.org/10.1029/2006WR005787

Cayocca, F. (2001). Long-term morphological modeling of a tidal inlet: the Arcachon Basin, France. Coastal Engineering, 42(2), 115-142. https://doi.org/10.1016/S0378-3839(00)00053-3

Charru, F., Andreotti, B., and Claudin, P. (2013). Sand ripples and dunes. Annual Review of Fluid Mechanics, 45, 469-493. https://doi.org/10.1146/annurev-fluid-011212-140806

Chou, Y. J., and Fringer, O. B. (2010). A model for the simulation of coupled flow-bed form evolution in turbulent flows. Journal of Geophysical Research: Oceans, 115(C10). https://doi.org/10.1029/2010JC006103

Cortese, T. A., and Balachandar, S. (1995). High performance spectral simulation of turbulent flows in massively parallel machines with distributed memory. International Journal of High Performance Computing Applications, 9(3), 187-204. https://doi.org/10.1177/109434209500900302

Jerolmack, D. J., and Mohrig, D. (2005). A unified model for subaqueous bed form dynamics. Water Resources Research, 41(12). https://doi.org/10.1029/2005WR004329

Kennedy, J. F. (1969). The formation of sediment ripples, dunes, and antidunes. Annual Review of Fluid Mechanics, 1(1), 147-168. https://doi.org/10.1146/annurev.fl.01.010169.001051

Kidanemariam, A. G., and Uhlmann, M. (2014). Direct numerical simulation of pattern formation in subaqueous sediment. Journal of Fluid Mechanics, 750, R2. https://doi.org/10.1017/jfm.2014.284

Kidanemariam, A. G., and Uhlmann, M. (2017). Formation of sediment patterns in channel flow: minimal unstable systems and their temporal evolution. Journal of Fluid Mechanics, 818, 716-743. https://doi.org/10.1017/jfm.2017.147

Langlois, V., and Valance, A. (2007). Initiation and evolution of current ripples on a flat sand bed under turbulent water flow. The European Physical Journal E, 22(3), 201-208. https://doi.org/10.1140/epje/e2007-00023-0

Marion, A., Bellinello, M., Guymer, I., and Packman, A. (2002). Effect of bed form geometry on the penetration of nonreactive solutes into a streambed. *Water Resources Research*, *38*(10), 27-1. doi:10.1029/2001WR000264

McLelland, S. J., Ashworth, P. J., Best, J. L., and Livesey, J. R. (1999). Turbulence and secondary flow over sediment stripes in weakly bimodal bed material. Journal of hydraulic engineering, 125(5), 463-473. https://doi.org/10.1061/(ASCE)0733-9429(1999)125:5(463)

Meyer-Peter, E., and Müller, R. (1948). Formulas for bed-load transport. IAHSR 2nd meeting, Stockholm, appendix 2. IAHR.

Nezu, I., and Nakagawa, H. (1984). Cellular secondary currents in straight conduit. Journal of hydraulic engineering, 110(2), 173-193.

Nikuradse, J. (1933). Gesetzmäßigkeiten der turbulenten Strömung in glatten Rohren (Nachtrag). Forschung auf dem Gebiet des Ingenieurwesens A, 4(1), 44–44. https://doi.org/10.1007/BF02716946

Ouriemi, M., Aussillous, P., and Guazzelli, E. (2009). Sediment dynamics. Part 1. Bed-load transport by laminar shearing flows. Journal of Fluid Mechanics, 636, 295-319. https://doi.org/10.1017/S0022112009007915

Packman, A. I., Salehin, M., and Zaramella, M. (2004). Hyporheic exchange with gravel beds: basic hydrodynamic interactions and bedform-induced advective flows. *Journal of Hydraulic Engineering*, *130*(7), 647-656. 10.1061/~ASCE!0733-9429~2004!130:7~647!

Paull, C. K., Ussler III, W., Caress, D. W., Lundsten, E., Covault, J. A., Maier, K. L., ... and Augenstein, S. (2010). Origins of large crescent-shaped bedforms within the axial channel of Monterey Canyon, offshore California. Geology, 6(6), 755-774. https://doi.org/10.1130/GES00527.1

Shringarpure, M., Cantero, M. I., and Balachandar, S. (2012). Dynamics of complete turbulence suppression in turbidity currents driven by monodisperse suspensions of sediment. Journal of Fluid Mechanics, 712, 384-417. https://doi.org/10.1002/jgre.20142

Sotiropoulos, F., and Khosronejad, A. (2016). Sand waves in environmental flows: Insights gained by coupling large-eddy simulation with morphodynamics. Physics of Fluids, 28(2), 021301. https://doi.org/10.1063/1.4939987

Sun, R., and Xiao, H. (2016). CFD–DEM simulations of current-induced dune formation and morphological evolution. Advances in water resources, 92, 228-239. https://doi.org/10.1016/j.advwatres.2016.03.018

Stam, J. M. T. (1997). On the modelling of two-dimensional aeolian dunes. Sedimentology, 44(1), 127-141. https://doi.org/10.1111/j.1365-3091.1997.tb00428.x

Uhlmann, M. (2005). An immersed boundary method with direct forcing for the simulation of particulate flows. Journal of Computational Physics, 209(2), 448-476. https://doi.org/10.1016/j.jcp.2005.03.017

Venditti, J. G., Church, M. A., and Bennett, S. J. (2005). Bed form initiation from a flat sand bed. Journal of Geophysical Research: Earth Surface, 110(F1). https://doi.org/10.1029/2004JF000149

Wong, M., and Parker, G. (2006). Reanalysis and correction of bed-load relation of Meyer-Peter and Müller using their own database. Journal of Hydraulic Engineering, 132(11), 1159-1168. https://doi.org/10.1061/(ASCE)0733-9429(2006)132:11(1159)

Yalin, M. S. (2013). Mechanics of sediment transport. Pergamon press.

Zgheib, N., Fedele, J. J., Hoyal, D. C. J. D., Perillo, M. M., and Balachandar, S. (2018a). Direct numerical simulation of transverse ripples: 1. Pattern initiation and bedform interactions. Journal of Geophysical Research: Earth Surface. https://doi.org/10.1002/2017JF004398

Zgheib, N., Fedele, J. J., Hoyal, D. C. J. D., Perillo, M. M., and Balachandar, S. (2018b). Direct Numerical Simulation of Transverse Ripples: 2. Self-Similarity, Bedform Coarsening, and Effect of Neighboring Structures. Journal of Geophysical Research: Earth Surface. https://doi.org/10.1002/2017JF004399